The Aerodynamics of Axisymmetric Blunt Bodies Flying at Angle of Attack

Mark Schoenenberger, NASA
Prasad Kutty, Analytical Mechanics Associates
Eric Queen, NASA
Chris Karlgaard, Analytical Mechanics Associates

NASA Langley Research Center
1 N Dryden Street, MS 489
Hampton, VA 23681

***Abstract*—The Mars Science Laboratory entry capsule is used as an example to demonstrate how a blunt body of revolution must be treated as asymmetric in some respects when flying at a non-zero trim angle of attack. A brief description of the axisymmetric moment equations are provided before solving a system of equations describing the lateral-directional moment equations for a blunt body trimming at an angle of attack. Simplifying assumptions are made which allow the solution to the equations to be rearranged to relate the roll and yaw stability with sideslip angle to the frequency of oscillation of the vehicle body rates. The equations show that for a blunt body the roll and yaw rates are in phase and proportional to each other. The ratio of the rates is determined by the static stability coefficients and mass properties about those axes. A trajectory simulation is used to validate the static yaw stability parameter identification equation and a simple method of identifying the oscillation frequency from the body rates. The approach is shown to successfully extract the modeled yaw stability coefficient along a simulated Mars entry. Mars Science Laboratory flight data results are presented from earlier work which indicate that results from both the validation case and flight data are in agreement with preflight predictions. A brief discussion of the dynamic stability is also provided. Trimming at a non-zero angle suggests that the typical axisymmetric models of the dynamic stability coefficients should be modified. However, further experimental or computational work must be done to separate damping due to body rates and wind relative rates before the correct lifting formulation would affect simulation results.**

TABLE OF CONTENTS

1 NOMENCLATURE 1
2 INTRODUCTION 1
3 EQUATIONS OF MOTION 3
4 DATA REDUCTION 8
5 CONCLUSIONS 10
6 ACKNOWLEDGMENTS 11
REFERENCES 11

1. NOMENCLATURE

Symbols

A	Sinusoid amplitude
a, b, c	Functional form coefficients
C_A	Axial force coefficient
C_{A_β}	Derivative of C_A with respect to β
C_{L_α}	Lift curve slope with respect to α
C_{l_β}	Roll stability with respect to β
C_{m_α}	Pitch moment slope with respect to α
C_N	Side force coefficient
C_{N_β}	Derivative of side force with respect to β
C_{n_β}	Yaw moment slope with respect to β
$C_{n_r} - C_{n_{\dot\beta}}$	Yaw damping coefficient
$\bar{C_{n_r}}$	Yaw damping about body axis
C_Y	Side force coefficient
d	Reference diameter
I_{xx}, I_{yy}, I_{zz}	Moments of inertia
I_{xy}, I_{yz}, I_{xz}	Cross products of inertia
m, m_{EV}	Vehicle mass
$N_{damping}$	Yaw damping moment
p, q, r	Body rates
p_o, r_o	Initial body rates (roll and yaw)
p_{osc}, r_{osc}	Oscillatory components of p and r
q_∞	Freestream dynamic pressure
r_c	Constant roll component
r_{fitted}	Sinusoid model fit to roll rate
S	Reference area
t	Time
V_∞	Freestream velocity
v_x, v_y, v_z	Velocity components
x_{ac}, y_{ac}, z_{ac}	Aerodynamic coordinate axes
x_{cg}, y_{cg}, z_{cg}	Center of gravity location
$x_{nose}, y_{nose}, z_{nose}$	Nose location

Greek

α	Angle of attack
α_o	Initial angle of attack
α_T	Total angle of attack
α_{Trim}	Trim angle of attack
β	Angle of sideslip
β_o	Initial angle of sideslip
β_{Trim}	Trim angle of sideslip
δ	Phase angle
ρ_∞	Freestream density
ϕ	Bank angle
ω	Oscillation frequency
ω_q	Pitch oscillation frequency
ω_r	Yaw oscillation frequency

2. INTRODUCTION

For planetary and Earth entry, blunt bodies of revolution have long been the geometry of choice for aeroshells used to slow payloads from hypersonic entry velocities to low supersonic or subsonic speeds where deceleration is augmented with parachutes and propulsion. Aeroshell heatshield designs have typically been made up of some combination of large-

978-1-4799-1622-1/14/$31.00

angle cone and blunt sphere sections. The forebody shape is typically driven by a combination of heating and stability requirements depending on entry velocity and the planet atmosphere profile. Backshell geometries are typically axisymmetric as well with the specific shape frequently driven by payload constraints. Often, these bodies of revolution are flown with the center of gravity (cg) aligned with the axis of symmetry and therefore trim at zero degrees total angle of attack. This symmetry simplifies how aerodynamic forces and moments are modeled in any flight simulations used for mission design and landing site targeting. The static forces and moments can be tabulated as functions of total angle of attack only and decomposed into six-degree-of-freedom coefficients (with angles of attack and sideslip as the independent variables) for use in simulation. Often the dynamic stability derivatives are modeled as functions of total angle of attack as well. In contrast, a conventional airplane requires that aerodynamic coefficients be described independently about and along the roll, pitch and yaw axes (or other convenient six degree-of-freedom coordinate system). When an axisymmetric vehicle uses a radial center of gravity offset to fly at an angle of attack, relative to the approaching wind, axisymmetry is broken and in some ways the aerodynamic coefficients must be described more like an airplane.

On August 5, 2012, the Mars Science Laboratory (MSL) entry vehicle successfully slowed the Curiosity rover during its entry, descent and landing in Gale crater on Mars. Both the aeroshell and entry architecture for MSL were derived from previous successful configurations used to land on Mars which have all been based on the Viking missions of the 1970's[1]. MSL was the first since Viking to use an offset center of gravity to fly a lifting trajectory. Like the Viking entry vehicles, a reaction control system was used to control the vehicle. In addition, MSL was the first to use the RCS system to fly a guided entry to land within a small landing ellipse on Mars. During the planning for and execution of the flight reconstruction, it became obvious that the flight mechanics of the MSL vehicle with its offset center of gravity are more complex than those of more recent Mars missions which had all flown ballistically with no cg offset. The MSL data reduction was the inspiration for the analysis in this paper and will be used as an example [2].

The full equations of motion provide the tools to understand the impact of the capsule flying at an asymmetric orientation relative to the approaching wind. The yawing moment equation is separated into a linearized system of equations for a blunt body flying at angle of attack. The re-expression of the moment equation is used to show how the yawing moment slope, C_{n_β}, is properly extracted from body rates, r and p, measured by an instrument like an onboard inertial measurement unit (IMU). The equations show that the natural pitch and roll oscillations are correlated, connected by the yaw and roll moment slopes, C_{n_β} and C_{l_β} and the moments of inertia about the roll and pitch axes. A flight simulation of the MSL entry is used to validate the method of extracting the yaw stability and reconstruction results of the MSL flight trajectory are presented as well. These cases provide examples of how a simple relation can accurately extract the yaw stability for a lifting blunt body from measured body rates.

Like the static moments, the pitch and yaw damping coefficients should be modeled asymmetrically for a lifting flight. Unfortunately, it is very difficult to measure or compute the separate contributions to damping from rotational rates

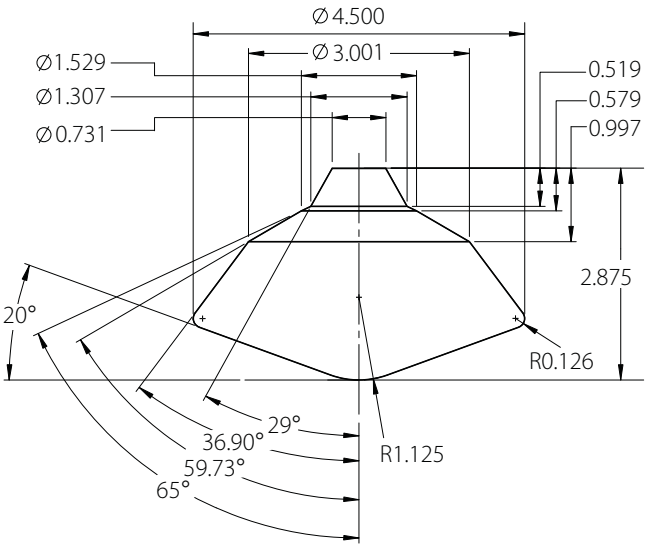

Figure 1. MSL entry vehicle dimensions

about the body and wind-relative axes. This will be briefly discussed below. For blunt bodies the damping moments are small compared to traditional aircraft which have long moment arms from the center of gravity and large aerodynamic surfaces that resist rotational motion. While small, the damping characteristics can have significant impact on blunt vehicle dynamics, especially for vehicles without a control system. Analysis described briefly below found that better measurements or predictions of blunt body damping derivatives are required before a correct implementation of the damping terms in simulation will have any significant influence of capsule damping predictions.

Mars Science Laboratory Entry Vehicle

The Mars Science Laboratory entry, descent, and landing (EDL) reconstruction was the genesis of the analysis presented here. Therefore, the MSL entry vehicle geometry is used here as an example of a blunt body of revolution flown at angle of attack where some axisymmetric assumptions are no longer valid. The MSL entry vehicle consists of a 4.5 meter, 70° sphere-cone heatshield with a backshell made of a series of truncated cones. The vehicle geometry and reference parameters are described in Figure 1 and the aerodynamic coefficient and coordinate system definitions are shown in Figure 2. The capsule dimensions shown in Figure 1 are simplified, but sufficient for describing the geometry of the flight vehicle. The design and measured diameters (and projected areas based on those diameters) show how the capsule design and what was fabricated changed slightly from the original specifications, set early in the project. The mass listed here is for the fully fueled entry vehicle, measured before launch. Some representative details of the MSL entry are described in later sections as the lateral-directional equations of motion are applied to simulation and flight data. For details of the vehicle's aerodynamic characteristics and the reaction control system used to control the vehicle

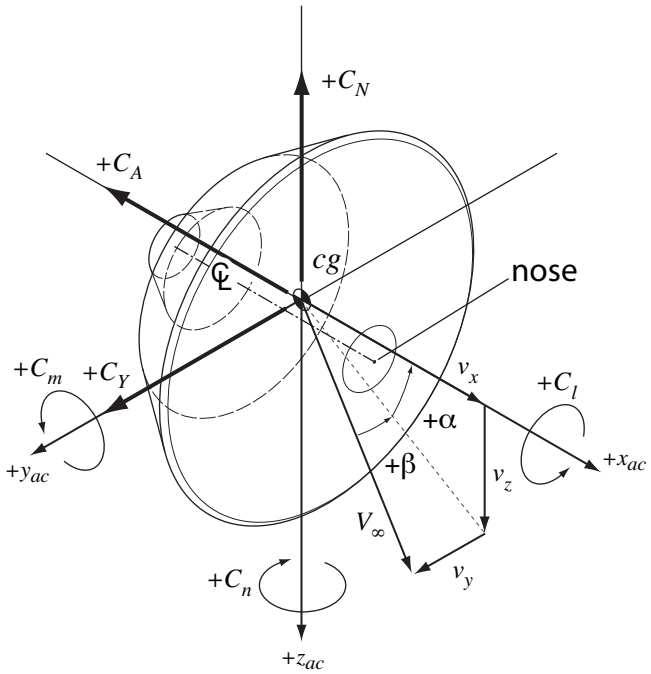

Key Geometric Locations
(in aerodynamic coordinate frame, *ac*)

Nominal	Measured
$x_{nose} = 0.0$	$x_{nose} = 0.0$
$y_{nose} = 0.0$	$y_{nose} = 0.0$
$z_{nose} = 0.0$	$z_{nose} = 0.0$
$x_{cg}/d = -0.300$	$x_{cg}/d = -0.295$
$y_{cg}/d = 0.0$	$y_{cg}/d = 0.0$
$z_{cg}/d = -0.0215$	$z_{cg}/d = -0.0221$

Figure 2. Blunt body coordinate system showing rates about body and wind axes.

and perform guided entry, refer to References [2], [3], [4], [5]. For a full report of the trajectory reconstruction and comparisons with preflight predictions of the aerodynamics, see References [6] and [7].

The moments of inertia of the entry capsule are

$$\begin{aligned} I_{xx} &= 4800\ kg - m^2 \\ I_{yy} &= 3800\ kg - m^2 \\ I_{zz} &= 2900\ kg - m^2 \end{aligned} \tag{1}$$

$$\begin{aligned} I_{xy}, I_{yz} &< 0.01 \cdot I_{zz} \\ I_{xz} &< 0.04 \cdot I_{zz} \end{aligned} \tag{2}$$

While approximate, these are representative of the values used in both the preflight simulation used later for validation and the measured values of the flight vehicle. Note that all cross products of inertia are small with the largest terms being less than four percent of any of the components in the trace of the inertia tensor. Most of the terms are less than one percent. This permits the longitudinal and lateral-directional equations to be decoupled and simplifies the terms of the equations developed below.

Figure 3 shows the angle-of-attack and angle-of-sideslip history of a preflight simulation of the MSL entry vehicle. Note that the trim angle starts near -16° (Mach > 30) and grows in magnitude to near -20°. The vehicle flies in a nose-down attitude because the lift of a blunt body comes mainly from the axial force component. Pointing nose-down directs the axial component of aerodynamic force upwards, producing positive lift for guided entry. Near Mach 2.5, the vehicle jettisons six balance masses to move the cg to the vehicle centerline and null the trim angle in preparation for a safe parachute deploy below Mach 2.0. The mass jettison event was colloquially referred to as the "straighten up and fly right" or SUFR maneuver. The sideslip trim angle remained close to zero.

During entry the guidance system commanded RCS jet firings in two primary modes. The first is Range Control where the reaction control system performs a series of bank reversals to modulate the lift vector to fly to an accurate downrange position. Near Mach 6, the vehicle entered the Heading Alignment phase where the control logic steered the vehicle directly toward the desired landing location, cleaning up any crossrange error incurred during the Range Control phase. The discrete moment impulses imparted by the reaction control jets when called to perform bank reversals and damp rates are detected by the IMU which complicates the data reduction process. This limited the areas where the stability derivatives could be extracted. The details of the data reduction process will be described in a later section.

The aerodynamics of blunt bodies used to fly a lifting trajectory are somewhere between the non-lifting, ballistic-entry variety and a full aircraft or spaceplane like the space shuttle Orbiter (as a point of reference, MSL flew at low lift-to-drag ratio of 0.24). Because the vehicle geometry is axisymmetric, the aerodynamic database is still generated as a function of total angle of attack (populated with computational fluid dynamics codes and ballistic range and wind tunnel data) and decomposed into components, but as will be shown there is lateral-directional coupling when flying at angle of attack much like an aircraft might see. The coupling is much more tenuous however, so the equations of motion can be simplified to yield practical analysis tools and relations between roll and yaw motions which would not be so "clean" for an aircraft. While the equations of motion used for the analysis done here are straight from classic documents, the authors believe this is the first explicit analysis of the static stability in this middle ground.

3. Equations of Motion

This section provides a brief overview of how the 6 degree-of-freedom (DoF) equations of motion were arranged to extract the yaw and roll stability with sideslip angle, β. There are many methods that have been used to identify aerodynamic coefficients from flight data. The method for extracting static stability described here was selected as it uses rate measurements taken directly from an onboard inertial measurement unit with no need for further integration or manipulation. No explicit attitude information is required, yet accurate values of the pitch and yaw stability can be measured and compared to preflight predictions to assess their accuracy. The rate data are used to extract static stability coefficients with very simple relations using only measured mass properties and the dimensions of the vehicle with the reconstructed dynamic pressure. The method is tolerant of many simplifying assumptions and can obtain accurate

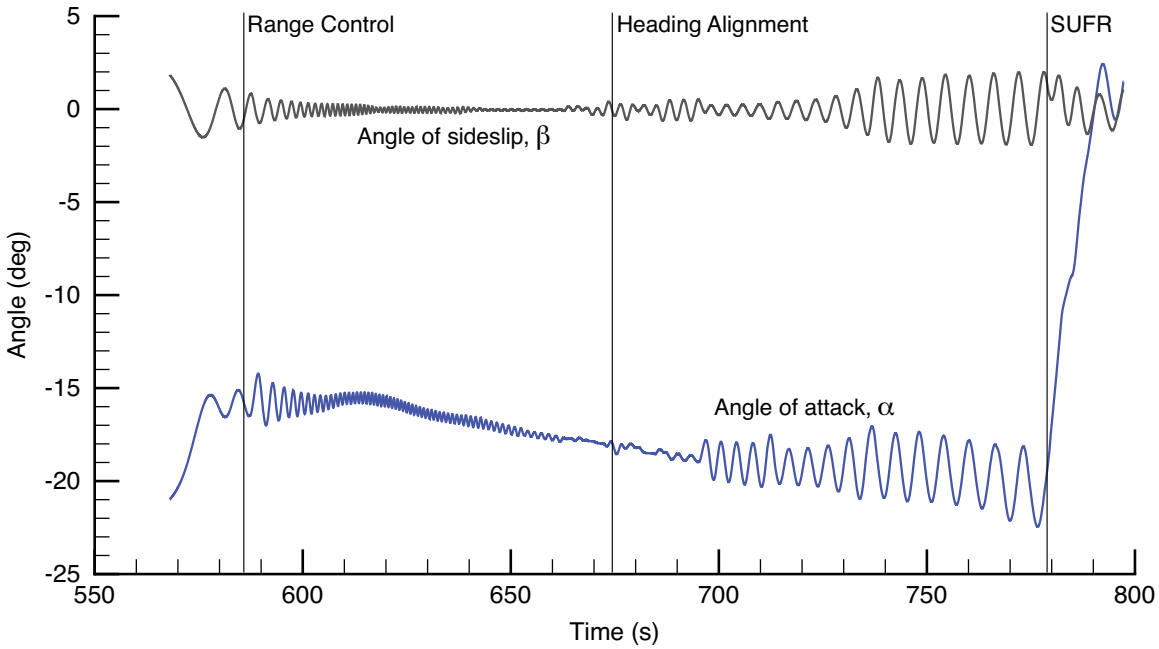

Figure 3. MSL preflight simulation results showing angles of attack and sideslip during entry with flight phases noted.

results very quickly and easily. When a vehicle trims at angle of attack, the process is a little more complicated and the simplifications introduce small errors in the reconstructed yaw stability. However the equations described here are useful tools for any blunt body entry data reduction process.

Assumptions

The equations of motion used in the derivations shown here and below are taken from the work of Duke, Antoniewicz and Krambeer [8]. There are a number of simplifying assumptions that can be made for blunt bodies that enable simple but accurate solutions to the equations of motion for use in extracting the stability coefficients. The equations shown here are linearized about the trim angle. For non-lifting bodies the trim angle is $\alpha_{Trim} = \beta_{Trim} = 0^\circ$ and for a lifting vehicle the equations are linearized about a non-zero trim angle, $\alpha = \alpha_{Trim}$ and $\beta_{Trim} = 0^\circ$. The amplitude of oscillation is assumed to be small. Also, as was shown to be valid for MSL, it is also assumed that the cross products of inertia are negligible. These assumptions allow the longitudinal and lateral-directional equations to be decoupled. For a blunt body traveling at hypersonic and supersonic speeds, gravity effects on the body rates are small over short segments of the trajectory. The change in dynamic pressure (or velocity and density) as a vehicle decelerates and descends through the atmosphere is assumed small over one or two cycles of oscillation. The contributions to angle of attack and sideslip due to the transverse accelerations from aerodynamic forces, including wind gusts are assumed small. The terms which contribute to these accelerations will be shown for completeness, before showing solutions with those terms omitted. The dynamic stability coefficients are assumed to be small, so terms in the moment equations proportional to the body rates are neglected. Over most of the trajectory the MSL vehicle was damped slightly or saw close to neutral dynamic stability and saw very little oscillation amplitude growth or decay during entry. Regardless, pitch damping does not contribute significantly to the oscillation frequency which is of primary interest here.

Longitudinal and General Non-lifting Capsule Oscillations

An axisymmetric blunt body with the center of gravity on the centerline and forward of the neutral point is statically stable and will tend to return to $\alpha_T = 0^\circ$ when displaced by any total angle-of-attack. As a convenience, an arbitrary coordinate system is typically placed on this axisymmetric vehicle, defining a pitch and yaw plane with three orthogonal forces and three orthogonal moments used to describe the net effect of aerodynamic pressures acting on the vehicle. If the cg is offset from the centerline, the vehicle will trim at an angle away from $\alpha_T = 0^\circ$ and produce lift. Refer back to Figure 2 for the coordinate definitions, angle-of-attack and angle-of-sideslip definitions, and aerodynamic coefficient definitions for the Mars Science Laboratory entry vehicle. Note that MSL flew with a radial cg offset. A nonlifting vehicle like a Mars Exploration Rover entry capsule has identical definitions, but with no radial cg offset.

For a vehicle with no cg offset, the equations describing the pitch and yaw moments are of the same form. For example the moment equation about the pitch axis is

$$\dot{\alpha} = q - \frac{\rho_\infty V_\infty S}{2m} C_{L_\alpha} \alpha \tag{3}$$

$$\dot{q} = \frac{q_\infty S d}{I_{yy}} C_{m_\alpha} \alpha \tag{4}$$

Omitting the heaving term in Equation 3 simplifies this system of equations into a single equation, that of an undamped harmonic oscillator. The solution becomes

$$\alpha = \alpha_o \cos(\omega_q t + \delta) \tag{5}$$

The frequency of oscillation is equal to

$$\omega_q = \sqrt{\frac{q_\infty S d}{I_{yy}} C_{m_\alpha}} \tag{6}$$

Which can be rearranged to extract the static stability

$$C_{m_\alpha} = -\frac{I_{yy}\omega_q^2}{q_\infty S d} \tag{7}$$

A similar equation can be derived for the yaw stability

$$C_{n_\beta} = \frac{I_{zz}\omega_r^2}{q_\infty S d} \tag{8}$$

Where ω_q and ω_r are the frequencies of oscillation of the pitch and yaw body rates. For small trim angles and small oscillations, these stability relations are of identical form and are equivalent. Differences in moments of inertia about the two axes would be the only reason the pitch and yaw frequencies might differ. For past Mars missions flying non-lifting trajectories [9], [10], [11], Equations 7 and 8 provided useful tools to assess the static stability and its variation along the trajectory using the body rates only.

For Mars Science Laboratory which flew at a non-zero trim angle the solution to the pitch stability equation is nearly identical to Equation 7. The difference being the oscillation amplitude is centered about the trim angle. The frequency of oscillation is still governed by the local pitch stability. The yaw equation becomes more complicated and will be described in the next subsection.

Lateral-Directional System of Equations

At angle of attack, the $\dot{\beta}$ axis of rotation is no longer aligned with the body yaw axis. Figure 4 shows the coordinate definition plot again, this time shown at the trim angle ($\beta = 0°$) with vectors representing the body and wind-relative rotation rates. Note the misalignment between $\dot{\beta}$ and the body rates for the capsule at an angle of attack. This misalignment introduces a complication for extracting the yaw static stability coefficient, C_{n_β}. A vehicle like MSL typically flies with an onboard IMU and records the body rates, p, q, and r. In the case of MSL this data is used for real-time navigation during entry and saved for post-flight reconstruction. Angles of attack and sideslip are reconstructed using rate and acceleration data and in the case of MSL, surface pressure measurements. Here a system of equations describing the yaw and sideslip moments is solved to show how the roll, yaw and sideslip rates are all correlated with each other. This correlation is used to determine relations for identifying the roll and yaw stability coefficients.

Here a system of equations is defined describing the angular accelerations about the roll and yaw axes and the relationship between the sideslip and body rates. This matrix was derived from the equations described in the NASA document by Duke, Antoniewicz and Krambeer [8]. The equations are linearized about a trim angle of attack ($\alpha_{Trim} = \alpha_o$, $\beta_{Trim} = 0$). Note the coefficient subscripts in this matrix equation indicate partial derivatives with respect to β, p, and r.

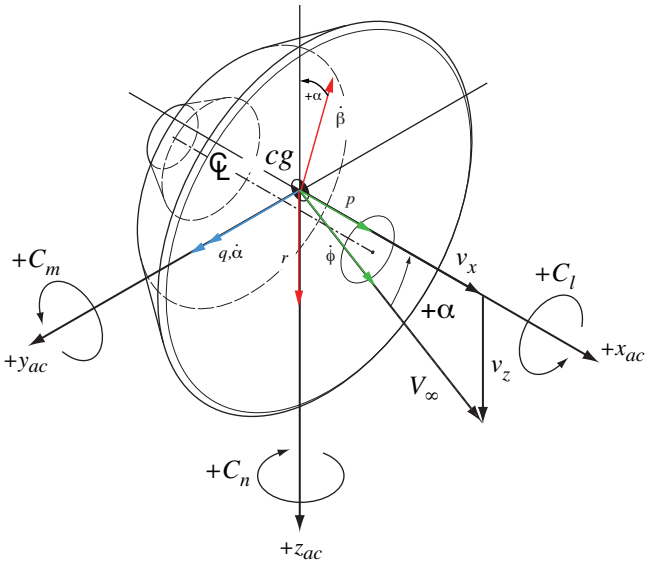

Figure 4. Body and wind relative rates

$$\begin{bmatrix} \dot{\beta} \\ \dot{p} \\ \dot{r} \end{bmatrix} = \begin{bmatrix} \dot{\beta}_\beta & \dot{\beta}_p & \dot{\beta}_r \\ \dot{p}_\beta & \dot{p}_p & \dot{p}_r \\ \dot{r}_\beta & \dot{r}_p & \dot{r}_r \end{bmatrix} \begin{bmatrix} \beta \\ p \\ r \end{bmatrix} \tag{9}$$

The intent here is to develop equations relating the frequency of oscillation to the static moments. As mentioned above, the damping coefficients are neglected as are the gravity and heaving terms. The terms remaining in these equations are then

$$\dot{\beta}_\beta = \frac{q_\infty S}{m V_\infty}(\sin\beta_o(C_{N_\beta}\sin\alpha_o + C_{A_\beta}\cos\alpha_o - C_Y) + \cos\beta_o(C_N\sin\alpha_o + C_A\cos\alpha_o + C_{Y_\beta})) \approx 0 \tag{10}$$

$$\dot{\beta}_p = \sin\alpha_o \tag{11}$$

$$\dot{\beta}_r = -\cos\alpha_o \tag{12}$$

$$\dot{p}_\beta = \frac{q_\infty S d}{I_{xx}} C_{l_\beta} \tag{13}$$

$$\dot{p}_p \approx 0 \tag{14}$$

$$\dot{p}_r \approx 0 \tag{15}$$

$$\dot{r}_\beta = \frac{q_\infty S d}{I_{zz}} C_{n_\beta} \tag{16}$$

$$\dot{r}_p \approx 0 \tag{17}$$

$$\dot{r}_r \approx 0 \tag{18}$$

Setting the contributions to $\dot{\beta}$ from the aerodynamic forces in Equation 10 to zero is an important assumption and required to obtain the clean solutions for roll and yaw stability below. Linearized about $\beta_o = 0°$, the first term is clearly zero. However, the contributions to $\dot{\beta}$ from the axial, normal and side forces, while small for a blunt body, would provide a more accurate expression for sideslip if accounted for. Neglecting this term does introduce some error to the expression for yaw and roll stability. This will be discussed below when comparing data reduction results from a validation case, but in short, this simplification does not add a large error.

These linear, state-space equations for the lateral-directional dynamics were transformed to a transfer function representation by applying the Laplace transform to Equation 9. The transfer function expression was conveniently solved through the inverse Laplace transform, yielding a time varying expression for sideslip and lateral-directional body rates. The resulting solution takes the form of a sinusoid with frequency ω, as given by

$$\beta(t) = \beta_o \cos\omega t + \left(\frac{p_o \sin\alpha_o}{\omega} - \frac{r_o \cos\alpha_o}{\omega}\right)\sin\omega t \tag{19}$$

$$\begin{aligned} p(t) = {} & \tfrac{\beta_o q_\infty Sd}{I_{xx}\omega} C_{l_\beta} \sin\omega t \\ & + \left[p_o - \tfrac{p_o \cos\alpha_o q_\infty SdC_{n_\beta}}{I_{zz}\omega^2} + \tfrac{r_o \cos\alpha_o q_\infty SdC_{l_\beta}}{I_{xx}\omega^2}\right]\cos\omega t \\ & + \left[\tfrac{p_o \cos\alpha_o q_\infty SdC_{n_\beta}}{I_{zz}\omega^2} - \tfrac{r_o \cos\alpha_o q_\infty SdC_{l_\beta}}{I_{xx}\omega^2}\right] \end{aligned} \tag{20}$$

$$\begin{aligned} r(t) = {} & \tfrac{\beta_o q_\infty Sd}{I_{zz}\omega} C_{n_\beta} \sin\omega t \\ & + \left[r_o - \tfrac{p_o \sin\alpha_o q_\infty SdC_{n_\beta}}{I_{zz}\omega^2} + \tfrac{r_o \sin\alpha_o q_\infty SdC_{l_\beta}}{I_{xx}\omega^2}\right]\cos\omega t \\ & + \left[\tfrac{p_o \sin\alpha_o q_\infty SdC_{n_\beta}}{I_{zz}\omega^2} - \tfrac{r_o \sin\alpha_o q_\infty SdC_{l_\beta}}{I_{xx}\omega^2}\right] \end{aligned} \tag{21}$$

Where β_o, p_o, and r_o are the initial sideslip, roll and yaw rates and ω is the oscillation frequency equal to

$$\omega = \sqrt{\frac{q_\infty Sd}{I_{zz}} C_{n_\beta} \cos\alpha_o - \frac{q_\infty Sd}{I_{xx}} C_{l_\beta} \sin\alpha_o} \tag{22}$$

The roll and yaw rate equations are of the form:

$$p = a_1 \cos\omega t + b_1 \sin\omega t + c_1 \tag{23}$$

$$r = a_2 \cos\omega t + b_2 \sin\omega t + c_2 \tag{24}$$

Next, the 2nd derivatives of these body rates in Equations 20 and 21 are equated with the first derivatives of the expressions of $\dot{p}$ and $\dot{r}$ in Equation 9. Using the expression for β in Equation 19 and rearranging yields two equivalent equations for the square of the natural frequency of pure sideslip oscillation:

$$\begin{aligned} \ddot{p} = \tfrac{q_\infty Sd}{I_{xx}} C_{l_\beta} \dot{\beta} &= \tfrac{q_\infty Sd}{I_{xx}} C_{l_\beta} (p \sin\alpha_o - r\cos\alpha_o) \\ &= -\omega^2 p + c_1\omega^2 = \omega^2(c_1 - p) \end{aligned} \tag{25}$$

$$\omega^2 = \frac{q_\infty Sd}{I_{xx}} C_{l_\beta} \left(\frac{p\sin\alpha_o - r\cos\alpha_o}{c_1 - p}\right) \tag{26}$$

and

$$\begin{aligned} \ddot{r} = \tfrac{q_\infty Sd}{I_{zz}} C_{n_\beta} \dot{\beta} &= \tfrac{q_\infty Sd}{I_{zz}} C_{n_\beta} (p \sin\alpha_o - r\cos\alpha_o) \\ &= -\omega^2 r + c_2\omega^2 = \omega^2(c_2 - r) \end{aligned} \tag{27}$$

$$\omega^2 = \frac{q_\infty Sd}{I_{zz}} C_{n_\beta} \left(\frac{p\sin\alpha_o - r\cos\alpha_o}{c_1 - r}\right) \tag{28}$$

Equations 26 and 28 are two expressions for the same frequency of oscillation common to the roll and yaw rates. Equating the two RHS terms in these equations and rearranging shows how the static stability coefficients and mass properties are correlated with the body rates.

$$\frac{r - c_2}{p - c_1} = \frac{C_{n_\beta}}{C_{l_\beta}} \frac{I_{xx}}{I_{zz}} \tag{29}$$

The constant terms in Equations 20 and 21 are equal to the coefficients c_1 and c_2. Comparing these terms reveals that the two constants are proportional to each other. Introducing another arbitrary constant, c_3 yields

$$c_1 = c_3 \cos\alpha_o \tag{30}$$

$$c_2 = c_3 \sin\alpha_o \tag{31}$$

Therefore, the constant components of the p and r rates that satisfy the system of lateral-directional system of equations are correlated. Substituting these rates into the $\dot{\beta}$ relation within Equation 9 shows that these constant rates are orthogonal to the sideslip rotational vector and represent the components of a pure bank ($\dot{\phi}$) about the velocity vector. Therefore the terms, $c_1 - p$ and $c_2 - r$ represent oscillatory components of the roll and yaw rates.

$$p_{osc} = p - c_1 \tag{32}$$

$$r_{osc} = r - c_2 \tag{33}$$

Note that any combination of persistent roll and yaw rates that do not meet the orthogonality relationship in Equations 30 and 31 would result in angle of attack oscillations and the longitudinal and lateral-directional equations would no longer be decoupled. For a vehicle that is banking, constant rates can be subtracted from the measured body rates to determine the oscillatory components. Once the constant rates have been subtracted, the remaining oscillatory parts of the roll and yaw rates are the components of a pure sideslip oscillation. Equation 29 becomes

$$\frac{r_{osc}}{p_{osc}} = \frac{C_{n_\beta}}{C_{l_\beta}} \frac{I_{xx}}{I_{zz}} \tag{34}$$

This expression is quite powerful. It says that the roll and yaw rates are correlated by the yaw and roll static stability coefficients and the moments of inertia about those axes. For a sideslip oscillation, the yaw and roll rates are in phase and differ by a constant scale factor. The stability coefficients can then be extracted from these body rates. For a non-banking case, Equation 28 is rearranged into an expression for the yaw stability:

$$C_{n_\beta} = -\frac{I_{zz}\omega^2}{q_\infty Sd} \frac{r_{osc}}{\dot{\beta}} = -\frac{I_{zz}\omega^2}{q_\infty Sd} \frac{1}{(\frac{p_{osc}}{r_{osc}} \sin\alpha_o - \cos\alpha_o)} \tag{35}$$

and likewise for roll stability

$$C_{l_\beta} = -\frac{I_{xx}\omega^2}{q_\infty Sd} \frac{p_{osc}}{\dot{\beta}} = -\frac{I_{xx}\omega^2}{q_\infty Sd} \frac{1}{(\sin\alpha_o - \frac{r_{osc}}{p_{osc}} \cos\alpha_o)} \tag{36}$$

Analysis of typical blunt capsules shows that the $\frac{p_{osc}}{r_{osc}} \sin\alpha_o$ term is small compared to the $\cos\alpha_o$ term for reasonable blunt body trim angles. For a very useful first order approximation, the yaw stability is scaled by the cosine of the trim angle for a given measured frequency.

$$C_{n_\beta} = \frac{I_{zz}\omega^2}{q_\infty Sd \cos\alpha_o} \tag{37}$$

This development of equations is shown to provide rigorous explanation of how the oscillatory rates are correlated and how constant body rates can be present as well. Equation 37 could also have been determined directly from Equation 22 by making the assumption that the C_{l_β} term was small. Also note that Equation 37 reduces to Equation 8 when $\alpha_o = 0°$.

Theoretically, the frequency can be extracted from a roll or yaw rate history measured as the frequency of both are the same and in phase. In practice, the yaw rate, r, has a greater amplitude, thus providing a stronger signal for more accurate identification of aerodynamic parameters. Equation 37 is a very simple relation between the yaw stability coefficient and the oscillation frequency of the body rate data, most easily extracted from the yaw rate, r. This equation for yaw stability is equal to Equation 8 scaled by the inverse of $\cos\alpha_o$. Accounting for heaving and gravity effects on the sideslip rate will alter and complicate this equation, more accurately capturing the relationship between the body and wind-relative oscillations, but complicating the data reduction process.

Yaw Damping

In addition to the static moments being complicated by the non-zero trim angle of attack, consider how the dynamic stability of a blunt body is modeled. The yaw damping moment has typically been modeled with the following relation (or something similar) for blunt bodies, regardless of trim angle.

$$N_{damping} = \frac{q_\infty Sd}{I_{zz}} (C_{n_r} - C_{n_{\dot{\beta}}}) \frac{(r - \dot{\beta})d}{4V_\infty} \tag{38}$$

As it is very difficult to separate the damping due to yaw rate from the damping due to sideslip rate, the damping coefficients have historically been lumped together and multiplied by the average of the yaw and sideslip rates (or one of the two selected over the other) to calculate the damping moments. As has been shown above, for a vehicle that trims at angle of attack, the axes of rotation for these two rates are not parallel, so this averaging is an additional approximation.

This issue has long been a problem for high angle-of-attack aircraft dynamic testing and modeling [12], [13]. For example, forced oscillation tests typically impose an oscillating yaw rate, r, to a wind tunnel model and extract a component of the lumped term

$$\bar{C_{n_r}} = C_{n_r} - C_{n_{\dot{\beta}}} \cos\alpha \tag{39}$$

A common practice for aircraft aerodynamic modeling is to drop the $C_{n_{\dot{\beta}}}$ term with the assumption that $\dot{\beta}$ is small [12]. This is consistent with an aircraft flying a coordinated turn where sideslip remains small as a turn is executed. Any extreme maneuvers are transient and not oscillatory, so even cases that see large sideslip rates do not experience oscillations over a long time where damped or undamped vehicle characteristics can drive oscillation growth.

In contrast, blunt entry vehicles have no large aerodynamic surfaces to damp rates. They can see persistent oscillations about the pitch and yaw axes that can produce significant amplitudes depending on the damping characteristics (often dynamically unstable at supersonic speeds). Therefore the $C_{n_{\dot{\beta}}}$ term can not be neglected especially at low speeds and in a windy environment where wind-relative and body rates can differ considerably. An extensive study was undertaken to improve how the yaw and sideslip damping coefficients were modeled for a vehicle like MSL, trimming at angle of attack. The analysis was hampered by the long-existing problem of having no practical method of separating the damping coefficients. While a mathematical expression was developed which more correctly implemented the damping coefficients similar to the static relations developed above, in simulation it was shown that the new mathematical formulation did not affect capsule dynamics appreciably. Until there is a method to separate C_{n_r} from $C_{n_{\dot{\beta}}}$ the authors found no compelling reason to deviate from the yaw damping implementation shown in Equation 38 even when flying at an angle of attack as MSL did.

4. DATA REDUCTION

Comparisons to preflight simulation and flight data are described below to show how the modifications to the axisymmetric assumptions enable the correct extraction of lateral stability of the capsule. Refer to papers by Karlgaard et al. and Schoenenberger et al. [6], [7] for a more detailed description of the reconstruction and comparisons with the preflight aerodynamic predictions.

Static Stability Identification Process

For the data reduction process used to compute C_{m_α} and C_{n_β}, segments of the vehicle yaw rate data were extracted at points along the trajectory where RCS jets were not firing. The selection of these quiescent periods ensured that the data being used to identify aerodynamic properties of the vehicle were taken from regions of the trajectory where the vehicle was subject to only aerodynamic forces (and gravity). In order to compute C_{n_β}, a range or window of yaw rate data was taken around each of these points and a sinusoid function of the following form was fitted to this "truth" signal:

$$r_{fitted} = A\cos(\omega t + \delta) + r_c \tag{40}$$

In this equation, A is the sinusoid amplitude, ω is the frequency of oscillation, δ is a phase shift and r_c is a constant offset representing any constant component of the yaw rate. A similar equation was fit to the pitch data to compute C_{m_α} and the angle-of-attack data to obtain the trim angle, α_o, used to compute C_{n_β} in Equation 37. A simple cost function was constructed to take the root sum square of the difference between the true yaw rate signal and the fitted signal calculated from Equation 40. An optimizer was used to find values of A, ω, δ and r_c that minimized the cost function producing the best fit to the true yaw signal. The length of the data window over which the signal was fitted was chosen to provide one to two oscillations of the sinusoid. Through this cost function minimization technique, the fitted pitch and yaw frequencies of oscillation were extracted and used to compute C_{m_α} and C_{n_β}.

Simple Simulation

Before data from a full entry simulation was used, a simple case was run approximating a ballistic range shot. Gravity was set to zero and a constant coefficient aerodynamic model was used so the pitch and yaw stability would be invariant across the simulation. This simulation was intended to provide a set of body rates generated from a trajectory in agreement with all the simplifying assumptions made in the development of the data reduction relations. The extracted parameters agreed very well with constant stability coefficients in the aerodynamic model. The change in dynamic pressure over the length of the sinusoidal wave segment fit to the rate data was one notable source of error remaining in the data reduction process. However, the error introduced by finding the mean frequency over a finite length of time was determined to be small. This method of identifying the frequency of oscillation from the rate data was selected as a reliable and robust technique. There are other methods that may produce more accurate results at a discrete point. Such improvements are left for later work.

Validation Simulation

A representative MSL trajectory was selected to validate the relationships between pitch and yaw static stability and the frequencies of oscillation given in Equations 7 (for a lifting vehicle) and 37. A preflight simulation provided flight dynamics, reaction control inputs and atmosphere and gravitational effects that very closely matched the actual flight trajectory with the benefit of having perfect knowledge of how the aerodynamic characteristics were modeled. Therefore, the extracted pitch and yaw stability values could be compared to "truth."

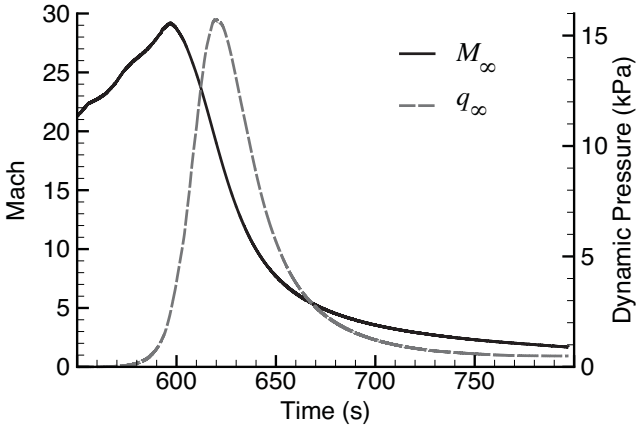

Figure 5. Mach and dynamic pressure profiles for MSL 12-GAL-01 simulation

Figure 5 shows the Mach and dynamic pressure profile for the preflight simulation 12-GAL-01. The name uses an internal MSL project convention and indicates this was the first simulation run in 2012 of a landing in Gale crater. Most conditions of this simulation are very close to those predicted to occur on the day of landing, so analysis of this simulation is representative of what was to be expected (and what in fact was measured) from flight telemetry. Early in the trajectory, Mach number is increasing both because of temperature variations in the rarefied segment of the atmosphere and because gravity is causing the capsule's planet-relative velocity to increase prior to entering the more dense "continuum" portion of the atmosphere. The peak deceleration occurs near Mach 16.

Figure 6 shows the roll, pitch and yaw body rates for the 12-GAL-01 simulation. The most obvious features of this plot are the bank reversals, indicated by the coordinated spikes in the roll and yaw rates. These maneuvers are executed during the range control phase of entry to modulate the lift vector in order to reach a targeted downrange location before entering the heading alignment phase. Starting near 690 seconds, the capsule enters heading alignment. Note the segments of small but constant roll rate, varying in sign during this phase. This is indicative of small residual bank rates as the capsule drifts between bank angle deadbands. RCS corrections fire when the capsule reaches a deadband leaving a residual bank rate in the opposite direction which is countered when reaching the other bank angle deadband. The large bank rate near the end of the entry profile is a 180° bank reversal performed to place the powered-landing descent-stage's radar system in the proper orientation for operation after heatshield separation and later separation of the rover/descent-stage from the aeroshell for landing. Also note the variation in pitch and yaw rate oscillation frequency with time. The variation is driven primarily by the dynamic pressure variation.

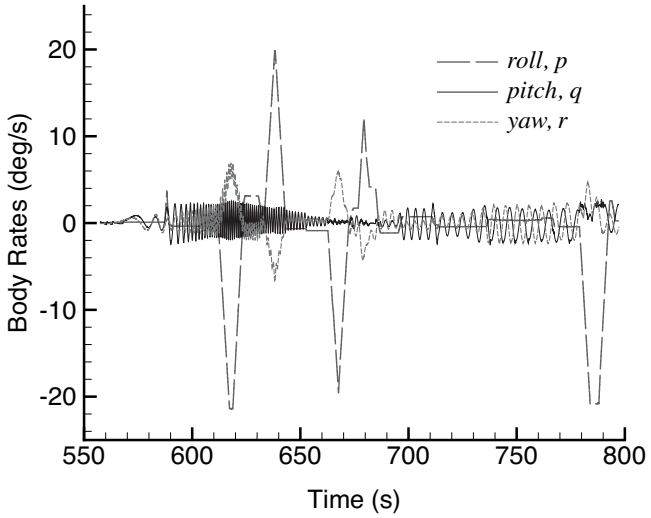

Figure 6. Body rates from MSL 12-GAL-01 simulation

The rates are shown here to show the raw data from which the parameters were extracted. As mentioned earlier, RCS firings cause large disruptions to the rate signals. The most obvious disruptions are the large bank reversals, but any small firing to damp rates or correct the bank orientation is enough to confuse the data reduction algorithm. Therefore, only segments containing a cycle or two free of RCS firings were considered for extracting the yaw stability. Nine segments of data were identified.

Figures 7a and 7b show two fits of the sinusoid function (Equation 40) to the yaw rates measured during two of the nine RCS-free trajectory segments. These fits show how closely the model agrees with the simulated rate data. Overall fits to each segment were very good and the extracted frequencies are very close to the mean frequencies in the simulation even when the amplitudes at each peak did not match. Based on differences between the body rate and fitted curve wavelengths measured at the mean amplitude, errors in frequency using this method range from less than 0.5% up to near 2% depending on the particular data segment. This results in a small error in the extracted parameters. A better functional form, perhaps accounting for the change in frequency due to deceleration, and/or amplitude change due to damping [14], might identify the frequency of oscillation more accurately. The constant amplitude sine wave was selected for robustness at the expense of the small residual fit error.

Figure 8 shows the extracted pitch and yaw stability coefficients identified at the centers of the nine data segments along the 12-GAL-01 simulated MSL entry trajectory. The local stability coefficients, calculated by finite difference from the MSL aerodynamic database, along the entire entry are plotted and the nine truth points corresponding to the extracted points are noted by symbols. Overall the agreement with the simulation data is very good. The extracted coefficients are within the same error margins for both the pitch and yaw stability. Some consecutive yaw stability coefficients extracted at points that occurred during the range control phase of entry (Mach 14.9, 8.2 and 6.6) were each approximately 3.5% lower than the database. Subsequent analysis showed that omitting the gravity terms in the $\dot{\beta}$ equation in this region resulted in the most noticeable error when compared with the

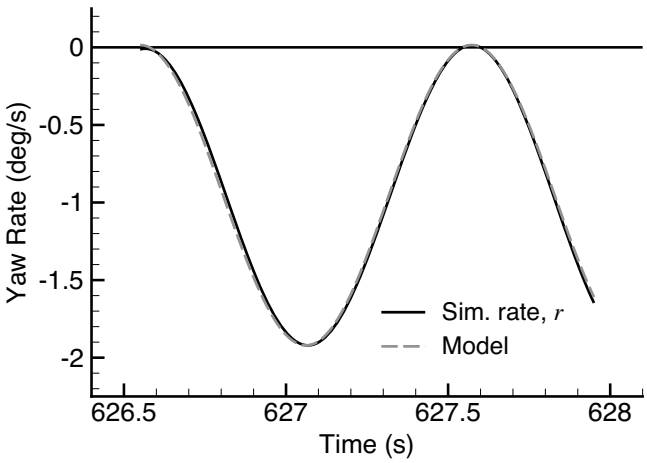

(a) Mach 14.9

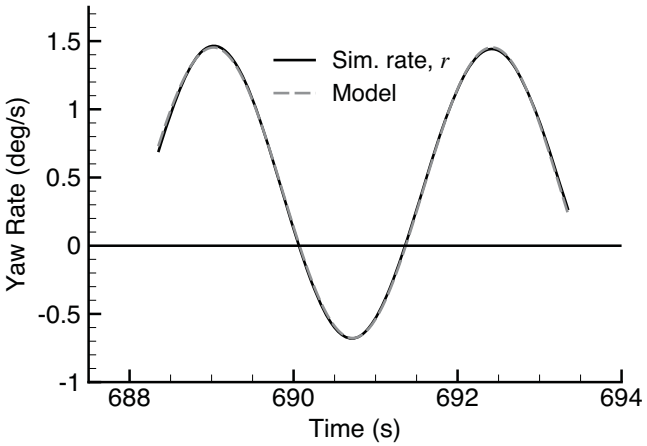

(b) Mach 3.9

Figure 7. Comparison of raw rate data to parameter identification model

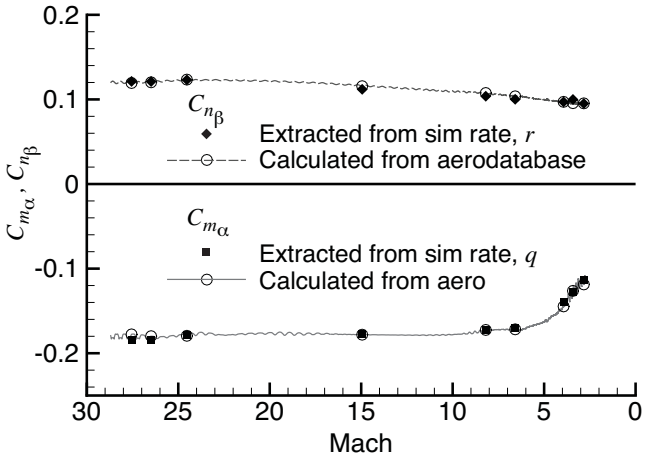

Figure 8. Validation of static stability method using MSL 12-GAL-01 simulation

simulation $\dot{\beta}$ history. The heaving terms did not appear to appreciably alter $\dot{\beta}$ for the MSL vehicle. Keeping the gravity terms would produce a more accurate solution to the system of equations, but the extraction of the yaw stability would no longer be dependent on the oscillation frequency only. A more complex analysis would be required to extract the yaw stability. The errors in this region provide an estimate of the accuracy limits when using the simplified relation. The correction to Equation 8 reflected in Equation 37 is the first-order effect of an axisymmetric capsule flying at a non-zero trim angle.

Mars Science Laboratory Flight Data

In the same manner as the validation case, the static stability coefficients were extracted from MSL flight data using Equations 7 and 37. Figure 9 shows the results as published in a paper by Schoenenberger et al. [7]. The RCS firing history during MSL's entry was less active than preflight predictions over much of the trajectory. However, there were small but frequent firing events early in the trajectory which meant fewer quiescent data segments in the hypersonic regime. Figure 10 shows representative examples of the rate data measured by the Descent Inertial Measurement Unit (DIMU) during entry compared to the data reduction functions to which the data were fit. The rate data were very clean and fitting the sinusoid was much like doing so with simulation data.

The data points in Figure 9 are plotted against stability coefficients predicted by the MSL aerodynamic database, queried along the reconstructed trajectory determined by Karlgaard et al. [6]. Agreement with the extracted data and the nominal database is excellent with errors very similar to the validation case. This indicates that flight data quality was very good and the preflight database closely predicted the stability characteristics of the capsule during all of entry.

As MSL trimmed at an angle of between $\alpha_{Trim} = -16^\circ$ and -20°, the correction to the axisymmetric equation for C_{n_β} removed an error of between 4 and 7% across the entry. This is important when evaluating the reconstructed data and comparing to preflight predictions and the uncertainty margins used in preflight trajectory and controller design. This improvement removes an error that would have been a significant fraction the of the $\pm 20\%$ static stability uncertainty carried in the MSL aerodynamic database [4]. Without the understanding provided by the formulations shown here, the MSL project may have recommended expanding the yaw stability uncertainties.

5. CONCLUSIONS

The Mars Science Laboratory entry vehicle was the first planetary spacecraft to fly a lifting trajectory since Viking and the first to fly a guided entry at another planet. Prior to MSL a series of axisymmetric vehicles flying ballistic trajectories were flown to Mars. Assessment of the flight performance of these vehicles was simplified because of the axisymmetric shape of the vehicle and the trim angle being close to a total angle of attack of 0°. The MSL capsule trimmed between -16° and -20° during its entry through the Mars atmosphere. Flying at this angle effectively changes the aerodynamic characteristics into those of a vehicle somewhere between an axisymmetric capsule and a traditional aircraft like the space shuttle Orbiter. One key aspect that changed was the static stability. Instead of describing the

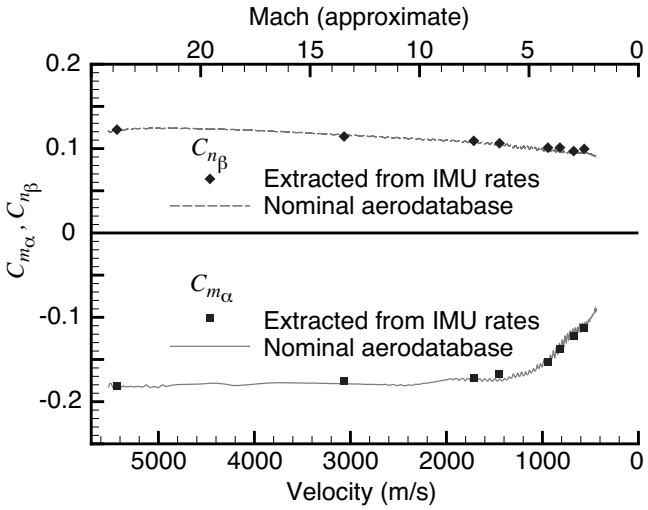

Figure 9. Comparison of flight stability coefficients to aerodatabase [7]

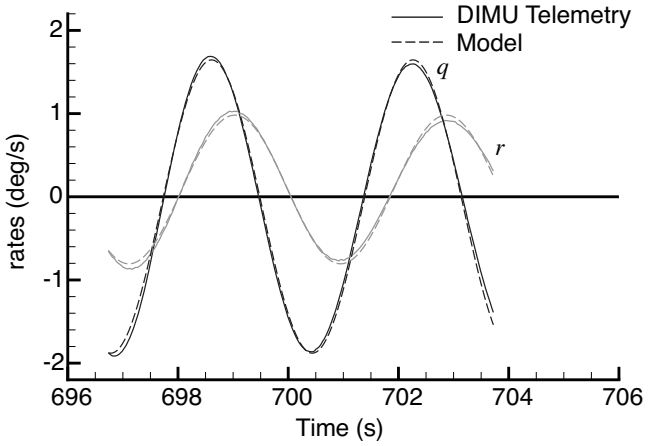

Figure 10. Comparison of parameter ID fit to measured MSL body rates at Mach 3.6 [7]

blunt body aerodynamics with two separate and orthogonal stability equations of the same form, MSL required longitudinal equations to describe the pitching motion and lateral-directional equations where roll and yaw motions are coupled. These equations were solved and several simplifying assumptions were made to yield simple expressions for the roll and yaw stability in terms of the frequency of oscillation common to the roll, yaw and sideslip rates.

The yaw stability equation was used to extract coefficients from a simulated MSL trajectory. Agreement between the extracted parameters and the aerodynamic database was good, with the omission of gravity terms being identified as the most significant source of error in this application. A solution of the full set of equations could be done to account for the dropped terms at the expense of the simple relation between static stability and frequency. Results for the flight data reconstruction, first reported in another paper [7], show extracted pitch and yaw stability coefficients in agreement with preflight predictions to within an accuracy very similar to the validation case run for this paper. The aerodatabase predicted the MSL static stability very well.

A brief discussion was included regarding how damping

coefficients might be more accurately implemented in simulations. As the symmetric static stability of blunt bodies of revolution is broken when flying at angles of attack, so too are the dynamic damping characteristics. This has long been an area of research for high angle-of-attack aircraft flight and is often limited by the lack of experimental capabilities for separating damping derivatives due to body and wind relative attitude rates. Analysis done in support of this paper indicated that without much better information about the differences between these damping derivatives, there is no significant benefit to altering the combined coefficients as is done with axisymmetric vehicles.

6. Acknowledgments

The authors would like to acknowledge Jeremy Shidner of Analytical Mechanics Associates at NASA Langley Research Center for his support in supplying flight simulation results used in the data reduction validation analysis. Mr. Shidner was a member of the MSL flight mechanics team and provided a great deal of assistance in transferring data to the authors as the data reduction methodologies were being developed.

References

[1] Ingoldby, R. N., Michel, F. C., Flaherty, T. M., Doty, M. G., Preston, B., Villyard, K. W., and Steele, R. D., "Entry Data Analysis for Viking Landers 1 and 2," TN–3770218, Martin Marietta Corp., Denver, CO, Nov. 1976.

[2] Dyakonov, A. A., Schoenenberger, M., and Van Norman, J. W., "Hypersonic and Supersonic Static Aerodynamics of Mars Science Laboratory Entry Vehicle," AIAA 2012-2999, 2012.

[3] Dyakonov, A. A., Schoenenberger, M., Scallion, W. I., Van Norman, J., Novak, L., and Tang, C., "Aerodynamic Interference Due to MSL Reaction Control System," AIAA 2009-3915, 2009.

[4] Schoenenberger, M., Dyakonov, A., Buning, P., Scallion, W., and Van Norman, J., "Aerodynamic Challenges for the Mars Science Laboratory Entry, Descent and Landing," AIAA 2009-3914, 2009.

[5] Schoenenberger, M., Yates, L., and Hathaway, W., "Dynamic Stability Testing of the Mars Science Laboratory Entry Capsule," AIAA 2009-3917, 2009.

[6] Karlgaard, C. D., Kutty, P., Schoenenberger, M., Munk, Michelle, M., Little, A., Kuhl, C., and Shidner, J., "Mars Entry Atmospheric Data System Trajectory and Atmosphere Reconstruction of the Mars Science Laboratory Entry, Descent and Landing," *Journal of Spacecraft and Rockets*, accepted for publication, 2013.

[7] Schoenenberger, M., Van Norman, J., Karlgaard, C., Kutty, P., and Way, D., "Assessment of the Reconstructed Aerodynamics of the Mars Science Laboratory Entry Vehicle," *Journal of Spacecraft and Rockets*, accepted for publication, 2013.

[8] Duke, E. L., Antoniewicz, R. F., and Krambeer, K. D., "Derivation and Definition of a Linear Aircraft Model," NASA RP– 1207, Aug. 1988.

[9] Spencer, D. A., Blanchard, R. C., Braun, R. D., Kallemeyn, P. H., and Thurman, S. W., "Mars Pathfinder Entry, Descent, and Landing Reconstruction," *Journal of Spacecraft and Rockets*, Vol. 36, No. 3, May-June 1999, pp. 357–366.

[10] Desai, P. N., Schoenenberger, M., and Cheatwood, F. M., "Mars Exploration Rover Six-Degree-of-Freedom Entry Trajectory Analysis," AAS 03-642, August 2003.

[11] Desai, P. N., Prince, J. L., Queen, E. M., Schoenenberger, M., Cruz, J. R., and Grover, Myron, R., "Entry, Descent and Landing Performance of the Mars Phoenix Lander," *Journal of Spacecraft and Rockets*, Vol. 48, No. 5, September-October 2011, pp. 798–808.

[12] Ogburn, M. E., Nguyen, L. T., and Hoffler, K. D., "Modeling of Large-Amplitude High-Angle-of-Attack Maneuvers," AIAA 1988-4357, 1988.

[13] Coe, P. L., Graham, A. B., and Chambers, J. R., "Summary of Information on Low-Speed Lateral-Directional Derivatives Due to Rate of Change of Sideslip," Tech. Rep. NASA TN D-7972, 1975.

[14] Schoenenberger, M. and Queen, E. M., "Limit Cycle Analysis Applied to the Oscillations of Decelerating Blunt-Body Entry Vehicles," NATO RTO-MP-AVT-152-006, 2008.

Mark Schoenenberger obtained his undergraduate degree in aerospace engineering and masters in fluid and thermal sciences at Case Western Reserve University in 1996 and 1998 respectively. Mark has worked at NASA Langley Research Center since then, starting as a contractor and becoming a civil servant in 1999. He was the lead aerodynamicist for the Mars Exploration Rover and Mars Science Laboratory entry vehicles. Mr. Schoenenberger was also the reconstruction lead for the MEADS experiment that flew on MSL.

Prasad Kutty received a B.S. in aerospace engineering from the University of Maryland in 2007. He has been with Analytical Mechanics Associates for six years. He has spent his first four years with the company at NASA Dryden Flight Research Center, providing flight dynamics and trajectory reconstruction support the Orion Launch Abort System Program, leading to the successful completion of the Pad Abort One flight test. Over the past two years , he has been a member of the Atmospheric Flight and Entry Systems Branch at NASA Langley Research Center where he has supported several entry, descent and landing projects including MSL, IRVE-3 and LDSD.

Dr. Eric Queen conducts research in the areas of guidance, control and simulation of aeromaneuvering spacecraft. He works in the Atmospheric Flight and Entry Systems Branch at NASA Langley Research Center. He has had a role in most of the U.S. Mars missions since Pathfinder, usually in support of entry, descent and landing. He is currently leading Langley's effort in support of EDL for the OSIRIS-REx asteroid sample return mission.

Christopher D. Karlgaard receive B.S. degrees in mathematics and aerospace engineering from the University of Maryland, and M.S. and Ph.D. degrees in aerospace engineering from Virginia Tech. He has been employed with Analytical Mechanics Associates, Inc. in Hampton, VA since June 2001 where he is currently a Supervising Engineer. His areas of expertise include Kalman filtering, state estimation and flight dynamics.